Effect of Cu on amorphization of a TiNi alloy during HPT and shape memory effect after post-deformation annealing**

By *Hamed Shahmir*, Mahmoud Nili-Ahmadabadi, Mahdi Mohammadi, Yi Huang, Mariusz Andrzejczuk, Małgorzata Lewandowska, Terence G. Langdon*

Abstract

A ternary TiNiCu memory alloy was subjected to high-pressure torsion (HPT) followed by post-deformation annealing (PDA) to study the effect of Cu (5 at.%) on amorphization after HPT processing and also the microstructural evolution and shape memory effect (SME) after PDA. The results show that even after 20 revolutions the ternary alloy contains nanocrystalline areas and the microstructure is not fully amorphous. An easier martensite to austenite transformation and minor remaining austenite in the ternary alloy are responsible for suppressing amorphization. PDA at 673 K provides nanocrystalline microstructures containing an R-phase with a minor martensitic B19' phase in the ternary alloy. The SME of this alloy after PDA is not as satisfactory as for the binary alloy processed through similar conditions because of the existence of a high volume fraction of the R-phase. Nevertheless, the total recovered strain of the ternary alloy after PDA for 30 min has a maximum value of 6.5%.

[*] *Hamed Shahmir Corresponding-Author, Mahmoud Nili Ahmadabadi, Mahdi Mohammadi*
E-mail:h.shahmir@ut.ac.ir
School of Metallurgy and Materials, College of Engineering, University of Tehran, Tehran, Iran
Hamed Shahmir,
Department of Mining and Metallurgical Engineering, Amirkabir University of Technology, Tehran, Iran
Yi Huang,
Department of Design and Engineering, Faculty of Science and Technology, Bournemouth University, Poole, Dorset BH12 5BB, UK
Mariusz Andrzejczuk and Małgorzata Lewandowska,
Faculty of Materials Science and Engineering, Warsaw University of Technology, Woloska 141, 02-507 Warsaw, Poland
Terence G. Langdon,
Materials Research Group, Faculty of Engineering and the Environment, University of Southampton, Southampton SO17 1BJ, UK
[**] *This work was supported by the National Elites Foundation of Islamic Republic of Iran and in part by the European Research Council under Grant Agreement No. 267464-SPDMETALS (TGL). A part of the work was carried out within the statutory funds of the Faculty of Materials Science and Engineering of Warsaw University of Technology (MA and ML).*

1. Introduction

The conventional shape memory effect (SME) comes from the thermoelastic martensitic transformation of the parent austenite phase (B2) to a low temperature martensitic phase (B19') which leads to a crystallographically reversible transformation [1-2]. It is well-known that SME materials exhibit the ability to return to their initial shape upon heating above the austenitic phase transformation temperature after deformation in a martensitic phase. The primary mechanism for deformation of the martensitic TiNi alloy is a martensitic reorientation in which one martensite variant grows due to other variants shrinking during loading and this produces high stresses that may appear in local sites on the interfaces between variants and on the grain interfaces. These local stresses may exceed the yield stress for dislocation slip and thereby promote intragranular plastic deformation. Generally, the strain appearing during the martensitic reorientation is recoverable whereas the plastic strain is not recoverable and produces a deterioration in the SME [2-4]. Therefore, producing an appropriate strength to prevent slip plays an important role in attaining an optimum SME. In practice, work hardening followed by annealing, grain refinement and alloy-hardening are important methods employed for TiNi alloys in order to improve the strength of the material and thus improve the SME [5].

High-pressure torsion (HPT) is an efficient processing procedure for producing significant grain refinement [6-8] and therefore increasing the critical stress for intragranular slip but nevertheless HPT processing leads to limited ductility and also diminishes the recoverable strain in TiNi shape memory alloys [9]. In principle, the reorientation of the martensite and the formation of a single variant during active deformation should be partially or even fully suppressed in very small grains or in heavily deformed microstructures of the TiNi alloys [10]. In addition, the formation of an amorphous phase during HPT processing [11-15] will lead to a deterioration in the SME in TiNi shape memory alloys [9].

Accordingly, short term post-deformation annealing (PDA) at an appropriate temperature provides a very important solution in removing this limitation in heavily and/or severely-

.0deformed alloys [16,17]. Short term PDA at 673 K leads to a crystallization of the amorphous phase and recrystallization of the severely-deformed crystalline phase in the TiNi alloy [18-20]. It is worth noting also that the formation of nanograins due to PDA followed by quenching can suppress the austenitic to martensitic (B19') phase transformation and promote the formation of an intermediate martensitic phase (R) having dimensions in the range of ~60-150 nm [21] where both of these changes affect the SME significantly [22,23]. It was proposed earlier that if crystallized nano-grains form after PDA then there will be a critical grain size of the primary austenite for the appearance of a fully-martensitic microstructure and this critical size will be about 150 nm [24]. It was also shown earlier that the nanocrystalline microstructures after PDA at 673 and 773 K followed by ice-water quenching contain B19' martensite together with an R-phase and it was suggested that very small grains and the existence of an R-phase are two important factors which both contribute to a superior SME [24]. High annealing temperatures and long annealing times may remove the R-phase but with a consequent deterioration in the SME due to grain growth and a decrease in the strength of the material. Short-term anneals for 10 min at 673 K or only 1.5 min at 773 K after 1.5 turns of HPT appear to be the optimum procedure with a maximum recovered strain of up to ~8.4% and an improvement of more than 50% by comparison with the solution annealed (SA) condition in the binary TiNi alloy [9].

The addition of Cu to the TiNi alloy and the replacement of Ni by Cu lead to a transformation temperature which is much less sensitive to compositional changes and therefore produces an easier control of the shape memory properties. In addition, it leads to a narrow transformation hysteresis and a lower martensitic yield strength. Another significant feature in adding Cu is that the transformation temperature is relatively high and above room temperature and this provides an opportunity to realize the shape memory effect around room temperature. It is also important to note that the addition of 5 at.% Cu cannot change the transformation route so that the normal B2-B19' occurs in this alloy [25,26].

It follows that the addition of Cu to a binary TiNi alloy produces many advantages and the behavior of a nanocrystalline TiNiCu alloy prepared by HPT processing followed by PDA may exhibit superior properties including an excellent SME. To date, no information is available on the effect of HPT processing on the ternary TiNiCu alloy and its shape memory behavior after PDA. Accordingly, the present research was initiated to systematically investigate the effect of HPT on the amorphization of a ternary TiNiCu alloy when processed through different numbers of rotations and various PDA conditions and to critically examine the microstructural evolution and the shape memory behavior of this alloy.

2. Experimental materials and procedures

The experiments were conducted using a TiNi-based alloy having a nominal composition of Ti-45at%Ni-5at%Cu, henceforth denoted as Ti45Ni5Cu. Full details on the alloying and sample preparation were reported earlier [9]. The alloy was solution annealed at 1123 K for 60 min followed by ice-water quenching. The disks for HPT processing had diameters of 10 mm and thicknesses of ~0.79-0.80 mm and they were subjected to processing at room temperature under quasi-constrained conditions [27, 28] using an applied pressure of P = 2.0 GPa, a rotation speed of 0.5 rpm and total rotations, N, of 1.5 to 20 revolutions.

Each processed disk was carefully polished to give a mirror-like quality. Measurements of the Vickers microhardness, Hv, were recorded using a hardness tester having a load of 100 gf and with dwell times of 10 s for each separate measurement. These microhardness measurements were recorded along randomly selected diameters within each disk with measurements taken at separations of 0.45 mm and with the local value of Hv then estimated at every point as the average of four separate hardness values. In order to study the phases, X-ray diffraction (XRD) was employed using Cu Kα radiation at 40 kV with a tube current of 30 mA. The measurements of XRD were conducted over an angular 2θ range from 30° to 50° with a step size of 0.02° and using a counting time of 9.6 s at every step. Circular areas of ~3 mm diameter were selected for XRD from near the edges of the disks.

Differential scanning calorimetry (DSC) was performed using a TA Q 100 DSC instrument with a liquid nitrogen cooling accessory in non-isothermal (scanning) experiments with a 10 K min^{-1} heating rate up to 773 K. Samples from near the edges of the disks were prepared for DSC analyses. The transformation temperatures were measured by DSC with the specimens heated quickly to 393 K, maintained at temperature for 5 min, cooled to 173 K, maintained at temperature for 5 min and then brought back to 393 K. The cooling and heating rates were 10 K min^{-1} during the thermal cycling.

Post-deformation annealing (PDA) was performed at 673 K in a vacuum furnace after HPT processing for various times from 10 to 120 min. The heating rate of specimens in the PDA was 120 K min^{-1} when measured after placing the specimen in the furnace. Foils for transmission electron microscopy (TEM) were prepared before and after PDA at 673 K for 30 min using a focused ion beam (FIB) Hitachi NB5000 FIB facility and Gentle Mill Technoorg Linda at 3 mm from the disk centres in the normal sections of the disks so that the normals of the images lie in the shear direction. All TEM micrographs were obtained using JEM 1200 JEOL and HD 2700 Hitachi microscopes.

The shape memory effect was studied by loading up to 8% and then unloading followed by heating to ~423 K by dipping in hot oil and then ice-water quenching. The loading and unloading was conducted using a SANTAM tensile machine with a load capacity of 2 kN and under initial strain rates corresponding to ~7.4×10^{-4} s^{-1}. Electro-discharge machining (EDM) was used to prepare miniature tensile specimens from near the edges of the HPT-processed disks and these specimens had gauge dimensions of $2.0 \times 0.6 \times 0.5$ mm^3.

3. Experimental results

3.1. Microhardness measurements after HPT

The Vickers microhardness measurements are shown in Fig. 1 where the values of Hv are plotted along each disk diameter for the Ti45Ni5Cu alloy after processing by HPT through from 1.5 to 20 turns and the hardness value in the SA condition is denoted by the lower dashed line. It

is important to note that individual error bars are not included on the various datum points for clarity but nevertheless the average error on each point was typically of the order of ~2%. The results indicate a significant increase in the hardness at the edges of the disks after 1.5 turns and then the hardness values at the peripheries of the disks increase from Hv ≈ 527 after 5 turns to a saturated hardness of Hv ≈ 550 after 10 turns. By contrast, the hardness values in the disk centers increase more gradually from the SA value of Hv ≈ 185 to a value of Hv ≈ 360 after 20 turns. Inspection of Fig. 1(a) shows clearly that the hardness gradually evolves across the disk diameters with increasing numbers of rotations but the exceptional difference between the hardness values at the edge and in the centres of the disks demonstrates that, even after 20 turns, it is not possible to produce a fully homogeneous hardness distribution. On the contrary, there remains a very small area, within a radius of 200 μm at the centre of each disk, which retains a relatively much lower hardness even after 20 turns.

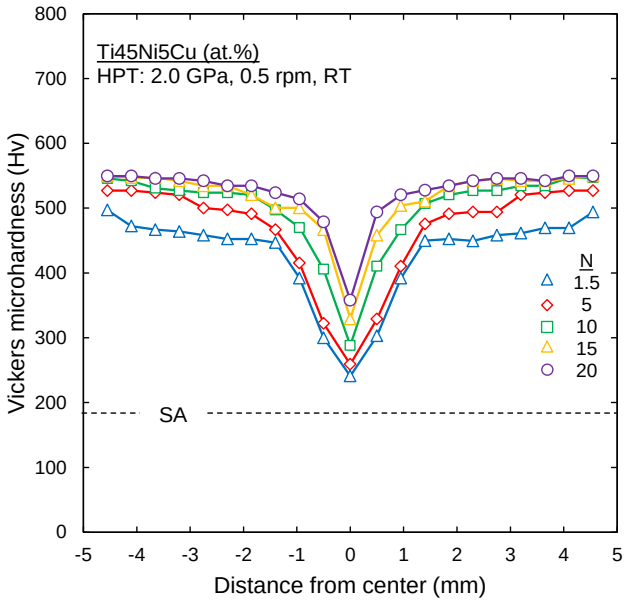

Fig. 1 Values of the Vickers microhardness versus distance from the center of the disk for Ti45Ni5Cu after HPT processing for various numbers of turns.

3.2. Microstructures before and after HPT

Measurements of the phase transformation temperatures, the thermal hysteresis and the

enthalpy of the austenite to martensite transformation were recorded for the SA alloy after ice-water quenching: these results are summarized in Table 1 where M_s and M_f are the martensite start and finish temperatures, A_s and A_f are the austenite start and finish temperatures, ΔT is the thermal hysteresis which is defined as the difference between the peak temperature of austenite to martensite on cooling and martensite to austenite on heating (A_p-M_p) and $\Delta H_{B19'\text{-}B2}$ is the martensite to austenite transformation enthalpy during heating. By quenching the solution annealed-ternary sample in ice-water (273 K), it is reasonable to anticipate that it will undergo a martensitic transformation (M_f = 299 K). In practice, the DSC results indicate that the A_s temperature is above room temperature (316 K) and this means that the martensite should be stable at room temperature in the alloy. However, the X-ray diffraction pattern of the Ti45Ni5Cu alloy in the SA condition represented in Fig. 2 shows ~16% retained austenite with the peak position corresponding to the $\{110\}_{B2}$ $2\theta \approx 42.20°$, calculated using standard methods [29], and it was shown earlier that the microstructure of the SA Ti49.8Ni alloy is fully martensitic. Data for Ti-49.8 at.% Ni was also added from an earlier investigation in Table 1 [15].

Table 1. The transformation temperatures M_s, M_f, A_s, and A_f (K), thermal hysteresis ΔT, T_0 (K) and average transformation enthalpy.

Alloy	M_s	M_f	A_s	A_f	ΔT	$\Delta H_{B19'\rightarrow B2}$ (J/mol)	Ref.
TiNi	316	299	331	348	35	1269	[15]
TiNiCu	311	275	316	342	30	1175	Present study

Figure 2 shows the X-ray diffraction patterns at the edges of the disks of the Ti45Ni5Cu alloy in the initial SA condition and after HPT for 1.5 to 20 turns. The results show clearly an intensive peak broadening and a decrease in the intensity of the martensitic peaks at the expense of increasing the austenitic peak in such a way that a broadened halo-like line, with a peak position corresponding to the $\{110\}_{B2(austenite)}$ 2θ, is dominant after processing by HPT up to 15

turns. This confirms the structural change from a strain-induced dislocation substructure to an amorphous structure and the martensite to austenite phase transformation during HPT processing.

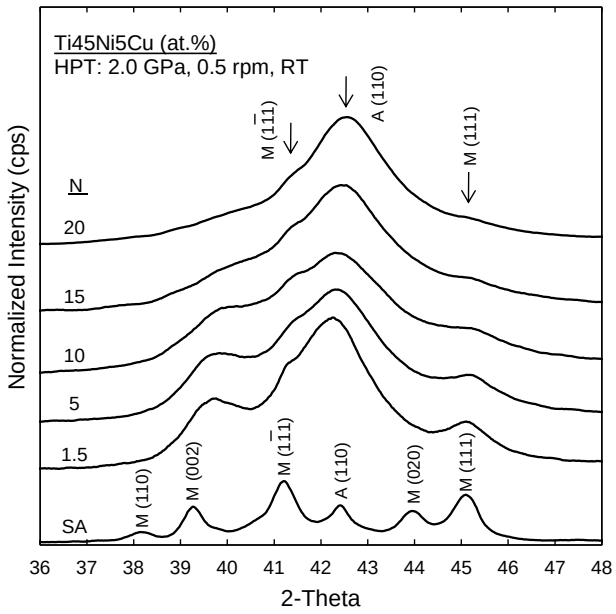

Fig. 2 X-ray patterns of Ti45Ni5Cu after solution annealing (SA) treatment and different conditions near the edges of the HPT-processed disks.

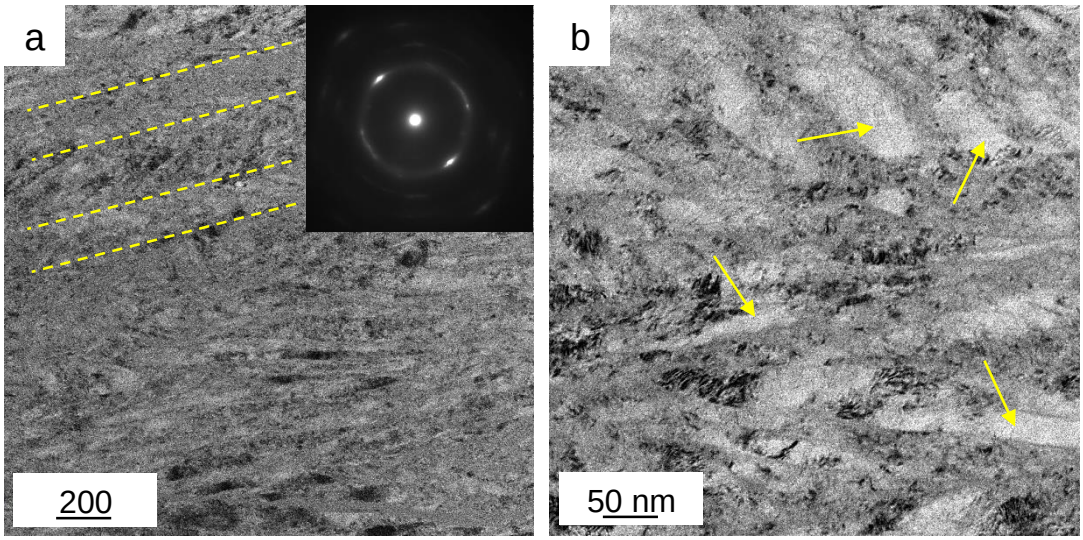

Fig. 3 TEM images and corresponding diffraction patterns of NiTiCu after 20 turns of HPT processing. (a,b) Severely deformed microstructure contains elongated nanocrystalline structure and shear bands marked by dashed lines. The band-shaped amorphous phases are marked by arrows. The arrangement of the diffraction spots in semi-continuous circles contains B2 (austenite) diffraction spots of the nanocrystallites.

The microstructure and a corresponding selected area electron diffraction (SAED) pattern are shown in Fig. 3 at a region ~3 mm from the disk centre after HPT through 20 turns for Ti45Ni5Cu. The microstructures in Fig. 3(a,b) reveal a mainly elongated nanocrystalline structure together with shear bands that are denoted by dashed lines. Most of the nanocrystalline structure shows dark contrast with respect to the band-shaped amorphous phases each with an average size of ~45 nm (as marked by arrows). The arrangement of the diffraction spots in semi-continuous circles in the SAED pattern of the Ti45Ni5Cu specimen in Fig. 3(a) confirms that the microstructure contains boundaries having high angles of misorientation with rings containing B2 (austenite) diffraction spots of the nanocrystallites.

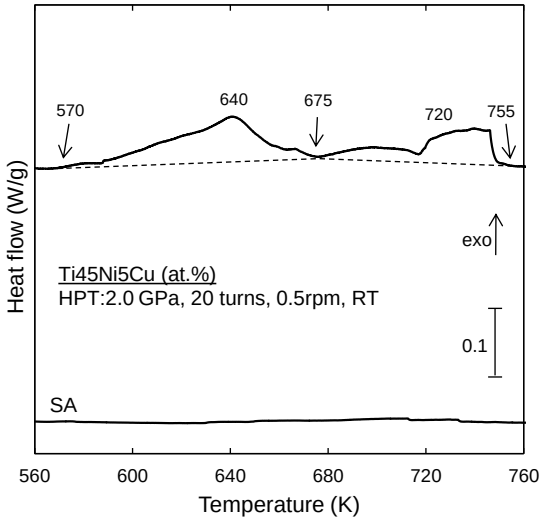

Fig. 4 Non-Isothermal (scanning) DSC measurement of Ti45Ni5Cu after solution annealing and HPT processing through 20 turns: the heating rate is 10 K min^{-1}.

Figure 4 shows non-isothermal DSC measurements at the edges of the HPT-processed disk through 20 turns and an initial SA sample. Two exothermic peaks are visible in the DSC thermogram after severe plastic deformation where the first and second peaks relate to a crystallization within the amorphous phase and a recrystallization of the remaining crystalline phase due to the formation of a complex microstructure containing a mixture of amorphous phase and any nanocrystalline austenite and martensite that remains present after HPT processing. Thus, these results indicate that the crystallization commences at ~560 K and thereafter the

samples are fully crystallized above ~660 K (at ~673 K which was selected as a PDA temperature) and then fully recrystallized above ~760 K. The stored energy is given by the integral of the two exothermic peaks for 20 turns and this value is estimated as ~1470 J mol^{-1}.

3.3. Microstructures and microhardness drop after PDA in the ternary alloy

Figure 5 shows the X-ray diffraction patterns for samples of the ternary alloy after HPT processing through 10 turns followed by annealing at 673 K for 10 to 60 min. A sharp R-phase peak, with the peak position corresponding to the $\{112\}_R$ $2\theta \approx 42.16°$, appears in the XRD patterns after annealing together with martensitic peaks suggesting the advent of crystallization and recrystallization. The calculated volume fractions of the R-phase after annealing are summarized in Table 2 based on the XRD results [29].

The TEM images in Fig. 6(a,b) show the HPT-processed disk after 10 turns followed by isothermal annealing at a temperature of 673 K for 30 min where it is clear that the crystallization is complete and it is apparent from the diffraction pattern in Fig. 6(c) that there are no diffuse rings corresponding to the amorphous phase. Thus, the microstructure of the ternary alloy after annealing contains an R-phase together with martensite and an estimated average size of the primary austenite grains of ~90 nm.

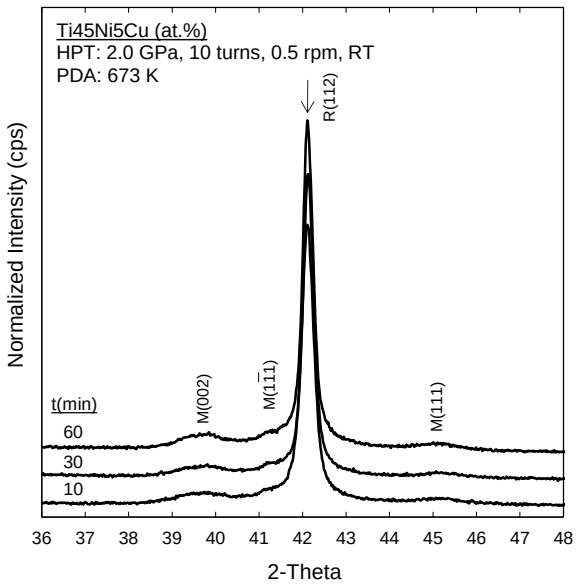

Fig. 5 X-ray patterns of Ti45Ni5Cu alloy after 10 turns HPT processing and PDA at 673 K and for various times.

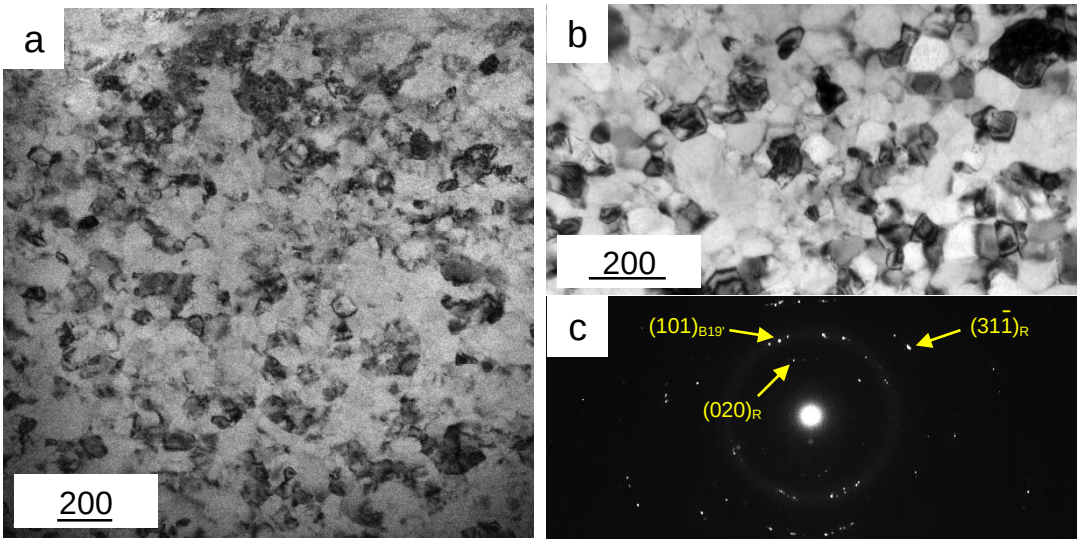

Fig. 6 TEM images and corresponding diffraction patterns of nanocrystalline TiNiCu alloy after 10 turns of HPT followed by PDA at 673 K for 30 min.

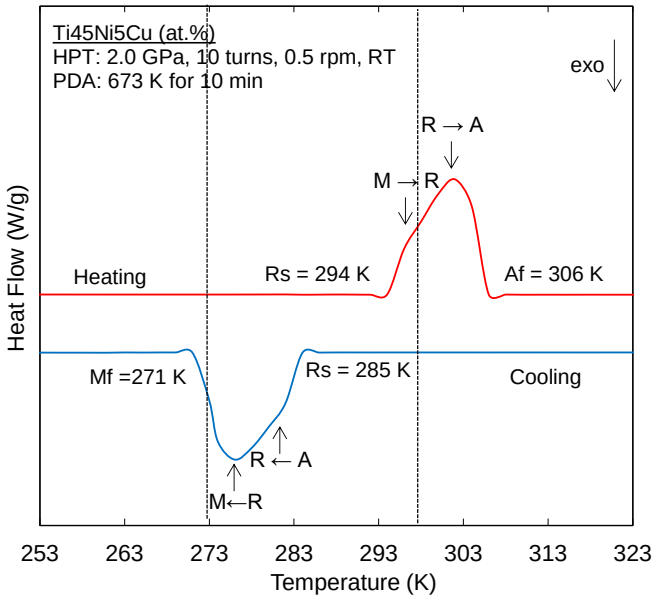

Fig. 7 DSC curves of Ti45Ni5Cu after 10 turns of HPT followed by PDA at 673 K for 10 min and further ice quenching. The quenching temperature of annealed sample and room temperature are shown by dashed lines.

Figure 7 shows typical DSC curves of the Ti45Ni5Cu alloy after 10 turns of HPT followed by PDA at 673 K for 10 min and further ice quenching. After solution annealing, a single stage transformation occurs on both the cooling and heating cycles (not shown). Nevertheless, after PDA a multi-stage transformation with two peaks appears on cooling and heating corresponding

to the transformation processes from austenite to the R-phase and further to martensite and the reverse path during cooling and heating, respectively. Since the annealed sample was quenched in ice-water at 273 K, shown by the vertical dashed line, it is expected that it will undergo a martensitic transformation but in practice the temperature is higher than M_f which indicates that the microstructure contains martensite and R-phase after quenching. The DSC result shows that room temperature at 298 K, denoted by the second vertical dashed line, is higher than R_s but lower than A_f and therefore it is concluded that the martensite and R-phase are stable at room temperature.

3.4. Shape memory investigations

Figure 8 represents stress-strain curves recorded for a characterization of the SME (a) for samples after PDA at 673 for various times after loading up to 6% and (b) for a sample after PDA at 673 for 30 min after different loadings up to 4, 6 and 8%. It is important to note that the recovered strain was measured after unloading and then heating the specimen to ~423 K by dipping in hot oil followed by ice-water quenching. The curve of the sample after loading up to 8%, indicated by the red line, shows a two-stage yielding which can be described by detwinning of R and B19' in the first stage and then a detwinning of B19', a stress-induced R→B19' transformation and also slip in the second stage. It is important to note that the microstructure of this sample includes R (71%) and B19' (29%) martensitic phases based on the XRD reults. It is apparent that 4.0% of stain is recovered by unloading due to elastic and also the pseudoelastic effect of the R-phase, 2.5% of stain is recovered by heating up to higher than the A_f temperature due to SME of B19' and 1.5% is a permanent strain due to slip and the introduction of dislocations. These results demonstrate that the total recovered strain is 6.5 which is a remarkable value for a shape memory alloy. The strain recovery of the specimens was measured and the data are summarized in Table 2 after loading to 8% where the results demonstrate that PDA at 673 K for 30 min is the optimum procedure for achieving a maximum shape recovery.

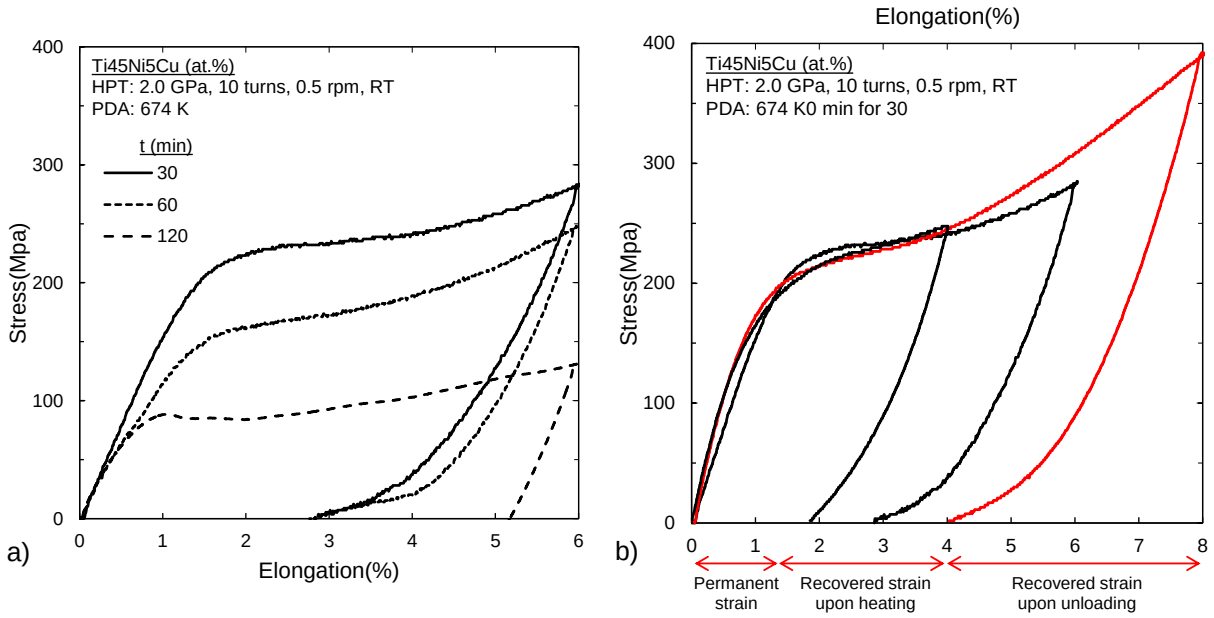

Fig. 8 Stress–strain curves of Ti45Ni5Cu after HPT processing for 10 turns followed by PDA at 673 K (a) for various times upon loading up to 6% and unloading, (b) for 30 min upon loading up to 4, 6 and 8% followed by unloading.

Table 2. The Vickers microhardness, volume fraction of R-phase and recovered strain of stress–strain curves after loading up to 8% (and 10% for some conditions) and unloading followed by heating to ~423 K for time for samples after HPT processing through 10 turns followed by annealing at 673 K for various times.

Alloy	Annealing time (min) at 673 K	Hv	R phase (%)	Flow stress at 6% (MPa)	Total recovered strain (%)	Ref.
Ti45Ni5Cu	10	310±8	73	-	-	Present Research
	30	301±5	71	279	6.5	
	60	295±3	64	237	6.3	
	120	252±2	-	125	6.0	
Ti49.8Ni	10	366±6	31	-	-	[9]
	30	340±7	29	292	7.6	
	60	304±2	22	270	7.8	
	120	274±2	18	260	6.9	

4. Discussion

4.1 Significance of Cu on amorphization during HPT

The microstructural evolution of binary TiNi alloys during HPT processing was studied earlier [11-15,30-32] but no information is available on the ternary TiNiCu after the same procedure. It was shown that HPT processing of a martensitic binary TiNi leads to the formation of a nanostructured phase due to grain fragmentation and also to amorphization by increasing the strain. Twin boundary movements are the most important deformation mode in martensitic TiNi alloys and in this activity the twinning divides the existing twin plates so that the twin boundaries act as obstacles for lattice dislocation slip and thus promotes the accumulation of dislocations and the formation of localized amorphous phases [33,34]. Basically, and due to the significant numbers of grain boundaries and twin boundaries which act as obstacles to dislocations, the martensitic microstructure promotes localized amorphization through local accumulations of dislocations [13,21]. The formation of shear bands during HPT processing also plays an important role in producing localized amorphization.

In the present investigation, it is clear that the formation of an amorphous phase in the ternary alloy has similarities to the behaviour in the binary alloy. However, even after 20 revolutions the ternary alloy contains nanocrystalline areas while the binary alloy is almost fully amorphous with a few remaining nanocrystals having sizes of only a few nanometers after HPT processing [15]. The appearance of the B2 phase is consistent with the XRD results in Fig. 2 and the SAED patterns in Fig. 3 and this indicates the occurrence of a reverse transformation from martensite to austenite induced by the severe plastic deformation. A comparison of the Ti45Ni5Cu and Ti49.8Ni results [15] reveals broader peaks in the Ti49.8Ni alloy which is probably due to the formation of a higher volume fraction of the amorphous phase. It has been reported that most of the nanocrystallites contain austenite whereas prior to HPT the crystalline structure was fully martensitic and generally a martensite-to-austenite and then a crystal-to-amorphous phase transformation are well known in binary alloys with increasing numbers of

rotations [14,15]. The present results clearly confirm essentially the same evolution in the ternary alloy but with some resistance against the formation of the amorphous phase with lower saturated hardness (~520 versus ~620 [15]) and stored energy (~1470 versus ~1530 J mol^{-1} [15]) in the saturation condition .

Since both the atomic radius and the number of valence electrons of the Cu are quite similar to those of Ni, the substitution of Cu for Ni has almost a minimal effect on the unit cell volume of the TiNiCu. It is assumed that supercells of Ti50Ni45Cu5 consist of five unit cells where only one atom of Ni is substituted by a Cu atom in each supercell [35]. It was reported that for the binary TiNi alloy the transformation strain of austenite to martensite is about 0.3% and for a ternary TiNiCu alloy, when the Cu addition is less than 7.7%, this transformation strain remains at about 0.3% since the transformation sequence is the same including B2 to B19' [10]. The peak position change due to the addition of 5 at.% Cu is about $2\theta \approx 0.2°$ which leads to a change in the lattice parameter below 0.01 Å. Therefore, the lattice constants of the B19' and B2 structures in Ti50Ni45Cu5 are very close to those of the equiatomic TiNi binary alloy. Accordingly, it is expected that the Ti45Ni5Cu and Ti49.8Ni alloys will show similar deformation mechanisms and hardening behavior. The microhardness results confirm this proposal since both alloys show an increment by a factor of ~2.5 after HPT processing through 20 turns. Nevertheless, the saturation levels of hardness in Fig. 1, the amounts of stored energy in Fig. 4 and the microstructures observations in Figs. 2 and 3 after HPT processing represent a difference between these two alloys after HPT.

The initial microstructure is a very important factor which affects the amorphization. Basically, the existence of austenite may delay the amorphization during HPT [14]. The initial microstructure of the Ti45Ni5Cu alloy contains ~16% austenite whereas the initial microstructure of the Ti49.8Ni alloy is full martensitic. In addition, the phase transformation temperatures, the values of ΔT and the enthalpy of the martensite to austenite transformation are higher for the binary TiNi alloy as shown in Table 1 which suggests an easier austenitic phase

transformation in the Ti45Ni5Cu ternary alloy. It is important to note that a similar behavior was reported for a TiNiFe (with 3 at.% Fe) ternary alloy in which the tendency to form the amorphous phase was low due to the alloy having a stable austenitic structure at room temperature [14].

It is possible to estimate the transformation temperature changes during the applied pressure of HPT processing by, following an earlier report [15], using the Clausius-Clapeyron relationship. Calculations show that with an applied pressure of 2.0 GPa the value of A_s decreases to ~13 K for the ternary alloy which promotes the austenitic phase transformation. In addition, heat evolution during the HPT processing is responsible for this transformation [15].

4.2 Microstructural evolution of the ternary alloy during PDA

The results in this investigation show that after 20 turns of HPT the microstructure contains nanocrystalline and amorphous phases with many boundaries which may act as nucleation sites due to the occurrence of heat-activated phenomena such as, for example, crystallization of the amorphous phase after PDA. It is important to note that this inhomogeneity affects further microstructural evolution during PDA and the formation of a range of grain sizes in the microstructures from ~30 to ~150 nm after PDA is an important consequence of this initial inhomogeneity. In addition, the DSC results show clearly that a dual phase of crystalline and amorphous phases exist as an inhomogeneity in the microstructure after HPT processing. The non-isothermal analysis suggests that crystallization and recrystallization start at 563 and 658 K, respectively. A significant drop of hardness as shown in Table 2, and the formation of sharp peaks in the XRD patterns in Fig. 4 after annealing at 673 K together with the TEM images in Fig. 6, confirm the occurrence of crystallization. These results indicate that the microstructure after PDA and ice-water quenching is R-phase together with a minor martensitic B19'. The appearance of the sharp peak of the R phase in the microstructure after annealing is interpreted by the suppression effect of the nanograins for the martensitic transformation and the formation of the B19' phase. It was reported that the R-phase is stable at grain sizes in the range of ~60-150 nm [21]. The present results demonstrate that the grain size in the sample after PDA at 673 K for

30 min is ~90 nm and this is within the range of ~60-150 nm so that the appearance of the R-phase in the diffraction pattern and the XRD results is consistent with this earlier report.

A grain size comparison of the ternary and binary alloys after identical PDA procedures shows a smaller grain size in the ternary alloy with ~90 nm versus ~140 nm [9]. It seems, therefore, that the driving force of crystallization/recrystallization in an almost fully amorphous binary specimen after HPT processing is higher than for the ternary specimen with a localized amorphous phase after a similar procedure. The higher energy storage in the material obtained by DSC analyses in Fig. 3 and the ultimate saturated level of hardness values in Fig. 1 also confirm this conclusion. Therefore, it is expected that heating of the fully amorphous structure will lead to more intensive coarsening.

4.3 The shape memory effect in the ternary alloy

It is well-known that a fully martensitic microstructure with appropriate strength will play an important role in producing the optimum SME [10]. It was found in earlier research that HPT processing of a binary TiNi alloy followed by the optimum PDA leads to an appropriate microstructure with an optimum grain size of primary austenite [9]. For clarity, the term optimum grain size means that it should not be too small either to suppress the martensitic transformation after quenching and/or to promote the austenite to R-phase transformation. In addition, the grain size should be sufficiently small to prevent grain growth and a strength drop. The present research shows the existence of large volumes of the R-phase and it appears not possible to remove the R-phase after PDA at 673 K even after an extensive annealing for 120 min. It is anticipated that annealing for an even longer time will promote softening of the material and a consequent drop in the critical stress due to an increase in grain size, thereby reducing the shape memory effect.

The R-phase plays an important role in the shape memory behavior of the specimens. Thus, this phase shows pseudoelasticity due to the stress induced R to B19' transformation and also SME but the available pseudoelasticity and shape memory strains are significantly lower than for the B19' phase which is very small (~1%). Therefore, it is reasonable to anticipate that the

existence of the R-phase within the microstructure will lead to a reduction in the SME [22,23]. The high value of the R phase promotes the pseudoelastic behaviour but diminishes the total recovered strain.

Inspections of the results presented in Fig. 8 and Table 2 indicate that the recovered strain for the nanocrystalline microstructure of the ternary alloy, obtained after annealing at 673 K for various times, is not as satisfactory as for binary alloys processed through similar conditions because of the existence of a high volume fraction of the R-phase. Nevertheless, the total recovered strain of the ternary alloy after PDA for 30 min has a maximum value of 6.5%.

Close inspection of Fig. 8(a) indicates that PDA for 120 min decreases the flow stress significantly and an intensive recovered strain is not obtained upon unloading in this condition by comparison with other PDA conditions. This is due to the larger grain size and therefore smaller amount of R-phase in this sample due to the longer annealing. However, this sample shows no significant shape recovery due to the drop in strength of the alloy after heating at 673 K for a long period.

5. Summary and conclusions

1. The ternary Ti-45at%Ni-5at%Cu alloy was processed by HPT through from 1.5 to 20 turns at room temperature. Microstructural examination revealed a resistance to the formation of an amorphous phase in the ternary alloy due to the easier martensitic to austenitic phase transformation and the remaining austenite in the initial condition of the ternary alloy.

2. Post-deformation annealing at 673 K leads to crystallization/recrystallization and the formation of nanocrystalline microstructures containing large volumes of R-phase with a minor martensitic B19' phase. The formation of nanograins suppresses the martensitic transformation and the formation of the B19' phase. It appears that a lower driving force of crystallization/recrystallization in the ternary specimen after HPT processing with a localized amorphous phase leads to the formation of a smaller grain size after PDA in the TiNiCu alloy.

3. The samples after PDA show stress-induced R to B19' transformations during loading

and significant portions of recovered stain by unloading due to the pseudoelastic effect of the R-phase. The shape memory effect of the ternary alloy after PDA is not as satisfactory as for binary alloys processed through similar conditions because of the existence of a high volume fraction (2.5%) of the R-phase. Nevertheless, the results show a total recovered strain of 6.5 for the ternary alloy after PDA for 30 min which is a remarkable value for a shape memory alloy.

References

1. C.M. Wayman, Introduction to Crystallography of Martensitic Transformations, New York: Macmillan, **1964**.

2 K. Otsuka, C.M. Wayman (eds), Shape Memory Materials, Cambridge University Press, Cambridge, U.K, **1999**.

3. K. Otsuka, K. Shimizu, *Int. Met. Rev.* **1986**, 31, 93.

4. E. Hornbogen, V. Mertinger, D. Wurzel, *Scr. Mater.* **2001**, 44, 171.

5. S. Miyazaki, Y. Ohmi, K. Otsuka, Y. Suzuki, *J. Phys. Colloq.* **1982**, 43 (C4), 255.

6. T.G. Langdon, *Acta Mater.* **2013**;61, 7026.

7. A.P. Zhilyaev, T.G. Langdon, *Prog. Mater. Sci.* **2008**, 53, 893.

8. R.Z. Valiev, D.V. Gunderov, A.V. Lukyanov, V.G. Pushin, *J. Mater. Sci.* **2012**, 47, 7848.

9. H. Shahmir, M. Nili-Ahmadabadi, Y. Huang, J.M. Jung, H.S. Kim, T.G. Langdon, *Mater. Sci. Eng. A* **2018**, 734, 445.

10. K. Otsuka, X. Ren, *Prog. Mater. Sci.* **2005**, 50, 511.

11. V.G. Pushin, V.V. Stolyarov, R.Z. Valiev, T.C. Lowe, Y.T. Zhu, *Mater. Sci. Eng. A* **2005**, 410, 386.

12. A.V. Sergueeva, C. Song, R.Z. Valiev, A.K. Mukherjee, *Mater. Sci. Eng. A* **2003**, 339:159.

13. T. Waitz, H.P. Karnthaler, *Acta Mater.* **2004**, 52, 5461.

14. S.D. Prokoshkin, I.Y. Khmelevskaya, S.V. Dobatkin, I.B. Trubitsyna, E.V. Tatyanin, V.V. Stolyarov, E.A. Prokofiev, *Acta Mater.* **2005**, 53, 2703.

15. H. Shahmir, M. Nili-Ahmadabadi, Y. Huang, T.G. Langdon, *J. Mater. Sci.* **2014**, 49, 2998.

16. R.Z. Valiev, A.V. Sergueeva, A.K. Mukherjee, *Scr. Mater.* **2003**, 49, 669.

17. Y. Huang, M. Lemang, N.X. Zhang, P.H.R. Pereira, T.G. Langdon, *Mater. Sci. Eng. A* **2016**, 655, 60.

18. N. Resnina, S. Belyaev, V. Zeldovich, V. Pilyugin, N. Frolova, D. Glazova, *Thermochimica Acta* **2016**, 627, 20.

19. H. Shahmir, M. Nili-Ahmadabadi, A. Razzaghi, M. Mohammadi, C.T. Wang, J.M. Jung, H.S.

Kim, T.G. Langdon, *J. Mater. Sci.* **2015**, 50, 4003.

20. H. Shahmir, M. Nili-Ahmadabadi, C.T. Wang, J.M. Jung, H.S. Kim, T.G. Langdon, *Mater. Sci. Eng. A* **2015**, 629, 16.

21. T. Waitz, V. Kazykhanov, H.P. Karnthaler, *Acta Mater.* **2004**, 52, 137.

22. S. Miyazaki, S. Kimura, K. Otsuka, *Philos. Mag. A* **1988**, 57, 467.

23. S. Miyazaki, K. Otsuka, *Metall. Trans.* **1986**, 17A, 53.

24. H. Shahmir, M. Nili-Ahmadabadi, Y. Huang, J.M. Jung, H.S. Kim, T.G. Langdon, *Mater. Sci. Eng. A* **2015**, 626, 203.

25. T.H. Nam, T. Saburi, K. Shimizu, *Mater. Trans. JIM* **1990**, 31, 959.

26. W. Tang, R. Sandström, Z.G. Wei, S. Miyazaki, *Metall. Mater. Trans. A* **2000**, 31A, 2423.

27. R.B. Figueiredo, P.R. Cetlin, T.G. Langdon, *Mater. Sci. Eng. A* **2011**, 528, 8198.

28. R.B. Figueiredo, P.H.R. Pereira, M.T.P. Aguilar, P.R. Cetlin, T.G. Langdon, *Acta Mater.* **2012**, 60, 3190.

29. B.D. Cullity, S.R. Stock, Elements of X-ray Diffraction, 3rd Ed, Englewood Cliffs, NJ, Prentice Hall, U.S.A, **2001**.

30. C. Rentenberger, T. Waitz, H.P. Karnthaler, *Mater. Sci. Eng. A* **2007**, 462, 283.

31. M. Peterlechner, T. Waitz, H.P. Karnthaler, *Scr. Mater.* **2008**, 59, 566.

32. M. Peterlechner, T. Waitz, H.P. Karnthaler, *Scr. Mater.* **2009**, 60, 1137.

33. J. Koike, D.M. Parkin, M. Nastasi, *J. Mater. Res.* **1990**, 5, 1414.

34. H. Nakayama, K. Tsuchiya, M. Umemoto, *Scr. Mater.* **2001**, 44, 1781.

35. L. Gou, Y. Liu, T.Y. Ng, *Intermetallics* **2014**, 53, 20.